Small-Scale Open-Circuit Wind Tunnel: Design Criteria, Construction and Calibration

Mauro S.*[a], Brusca S.[b], Lanzafame R.[a], Famoso F.[a], Galvagno A.[b] and Messina M.[a]

[a] *Department of Civil Engineering and Architecture, University of Catania, Viale A. Doria, 6, 95125, Catania, Italy.*
[b] *Department of Engineering, University of Messina, Contrada Di Dio, 98166, Messina, Italy.*
* Corresponding author

Orcid: /0000-0002-5377-7628

Abstract

The present paper deals with a study of very small-scale open-loop wind tunnel design and test. To verify the proposed design criteria, an open-circuit small-scale wind tunnel was built and tested. The designed wind tunnel is composed by a settling chamber, a contraction section, a test section, a diffuser as well as a fan. The test chamber has a squared cross section of 5 x 5 cm and an on-design flow velocity of about 6 m/s.

Particle Image Velocimetry was used to measure flow-field and flow main characteristics. Turbulence Intensity at different test chamber cross-sections was determined. The measured turbulence level was about 0.4 % at the test section entrance. A small increase in the turbulence intensity was registered along the test section. The obtained results were acceptable for a wind tunnel of that scale. Therefore, this wind tunnel may be used, for example, to test the flow-field around aerofoils.

A preliminary test on a NACA 0012 aerofoil was carried out. The result proved to be compatible with the aerodynamics theory as well as the scientific literature. Thus, the wind tunnel results may be used to calibrate and verify Computational Fluid Dynamics mathematical models.

Keywords: Wind tunnel design, Particle Imaging Velocimetry, low Re airfoils, micro wind turbines

INTRODUCTION

Nowadays Unmanned Air Vehicle (UAV), Micro Air Vehicle (MAV), as well as Micro Wind Turbine (MWT) are on the edge of the research in aerodynamics [[1]]. In these applications, wings, propellers and blades work at very low Reynolds Number. Therefore, low and very low Reynolds number aerodynamics has gained more attention due to increasing interest toward these applications [[1]].

At low Reynolds number flows, aerodynamics phenomena such as laminar separation bubble, may cause negative effects which lead to decreasing of lift and, at the same time, increasing of drag, thus reducing the stability of the vehicle and causing vibration and noise [[2] − [4]].

Moreover, 1D/3D numerical studies, about aerofoil behaviour in several sectors, need data for the calibration and validation. Over the past decades, some studies proved the capability of mathematical models for aerofoil simulations at high and low Reynolds numbers [[5], [6], [7]]. Sarlak et al. [[8], [9]] showed the potentiality of LES and RANS models for simulations of aerofoil aerodynamics at low and moderate Reynolds numbers.

Aerofoil characteristics are determined experimentally using wind tunnels [[9], [11], [12]]. However, wind tunnel tests are expensive and, in large wind tunnels studies on aerofoils, are difficult especially when using optic techniques [[11], [12]].

Thus, the need of a small-scale wind tunnel specifically designed for aerofoils studies comes out. Therefore, the present paper deals with a study of very small-scale open-loop wind tunnel design and test. A wind tunnel qualification was carried out by means of particle image velocimetry technique. Turbulence intensity, mean velocity as well as velocity profiles in test section were determined.

DESIGN CRITERIA

In the present paragraph, a description of wind tunnel design criteria is provided [[13]]. An open-loop wind tunnel is composed by the following main components (see Fig. 1):

1. A settling chamber;
2. A honeycomb;
3. A series of screens;
4. A contraction;
5. A test chamber;
6. A diffuser;
7. A fan.

These components are strictly necessary in order to correctly run experiments. As far as the design procedure is concerned, the first component to be designed is the test section. The

choices made for the test section design influence the whole wind tunnel components design. In particular, the dimensions of the test chamber have a great impact on the wind tunnel overall dimensions. The bigger the test section, the bigger the wind tunnel dimensions.

Secondly, the nozzle is designed to have maximum flow acceleration without turbulence and avoiding flow separation. Thirdly, the choice of the wind tunnel fan can be made. Fourthly, the first diffuser is designed. At the end, the settling chamber with the honeycomb and screens are designed.
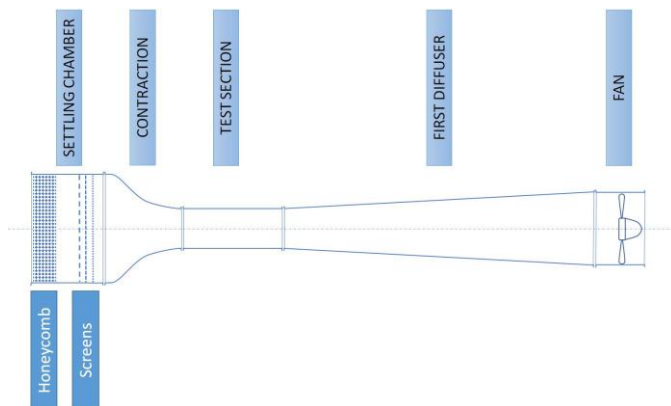
Figure 1: Open-circuit wind tunnel

Test section design

The test section design process starts from a priori project data: test chamber shape, main dimensions, and desired wind velocity. These parameters are strictly related to the kind of tests the wind tunnel is designed for.

The principal dimension of the test section is its hydraulic diameter which define the test chamber cross-sectional area.

$$\Omega_{TS} = \frac{\pi \, D_h^2}{4} \qquad (1)$$

Defining the test chamber cross-sectional area, Eq. (1) leads to hydraulic diameter calculation (2).

$$D_h = 2 \sqrt{\frac{\Omega_{TS}}{\pi}} \qquad (2)$$

According to Barlow [[14]], the test chamber length should be in the range $0.5 - 3$ times the hydraulic diameter in order to have almost uniform intake air flow (the air flow exiting the nozzle needs 0.5 times the hydraulic diameter to become uniform) and to avoid boundary layer separation at the test section exit (test chamber longer than 3 times the equivalent hydraulic diameter could cause an increase of the boundary layer thickness).

$$L_h = (0.5 \div 3) \, D_h \qquad (3)$$

A testing chamber length 2 times its hydraulic diameter is a good trade-off in the wind tunnel design.

As far as the testing section shape is concerned, a circular chamber cross-section without sharp edges is the best test chamber shape to avoid an increase in boundary layer thickness and possible air flow detaching.

On the contrary, a circular chamber cross-section is less practical. Therefore, a square testing chamber could be the best choice. To avoid air velocity reduction and boundary layer thickness increase at the sharp edges of the test chamber, the sharp edges should be rounded off. In this case, 45° chamfers are the best solution.

The test chamber is completed with flanges for the connection to the others wind tunnel sections and with observation windows for the use of measuring instruments.

Contraction design

The contraction section aims to accelerate the flow to the test chamber generating, at the same time, a uniform flow velocity profile. This wind tunnel section is the most difficult to design because the flow uniformity in the test chamber depends on this section design.

The nozzle design starts from its cross-section which has the same shape and dimensions of the testing chamber. In the case of square test chamber cross-section with 45° chamfers at the sharp edges, the nozzle exit section has 45° chamfers, as well.

In order to design the contraction inlet cross-section, it is necessary to define the nozzle area ratio. This parameter should be as large as possible to have the maximum flow acceleration and low total pressure losses in the upstream sections.

According to Bell and Metha [[15]], the nozzle cross-section area ratio should be in the range $6 - 10$. Using an area ratio less than 6 implies high pressure losses in the upstream wind tunnel component (screens), while an area ratio higher than 10 implies an excessive inlet cross-section dimensions. Therefore, a nozzle area ratio equal to 7 represent a good trade-off between dimensions and performance [[15]].

As far as the longitudinal-section nozzle profile is concerned, the nozzle silhouette is generated using the Bell-Metha fifth order polynomials [[15]]. Eq. (4) represents the mathematical equation of the Bell-Metha fifth order polynomials.

$$y = a_1 \, \xi^5 + a_2 \, \xi^4 + a_3 \, \xi^3 + a_4 \, \xi^2 + a_5 \, \xi + C \qquad (4)$$

In the polynomial of Eq. (4) the a_i are coefficients, while ξ is the ratio between x coordinate and the total nozzle length L (see Eq. (5)). In Eq. (4) $y = h$ is half cross-section side length.

$$\xi = \frac{x}{L} \qquad (5)$$

The x coordinate has the limits reported in Eq. (6).

$$0 \leq x \leq L \qquad (6)$$

In order to calculate Bell-Metha polynomial coefficients six equation are needed. These equations may be derived by imposing the boundary conditions (see Fig. 2). Two of these conditions may be obtained by imposing geometric conditions at nozzle inlet and outlet (Eq. (7) and Eq. (8)). Moreover, the nozzle shape has horizontal profile (null tangents values) in order to avoid flow detaching. This may be obtained by imposing the conditions in Eq. (9) and Eq. (10). At the same time, two inflection points are located at the nozzle inlet and outlet (null value of the second derivative of the Bell-Metha polynomial). These conditions are shown in Eq. (11) for the inlet section and Eq. (12) for the outlet.
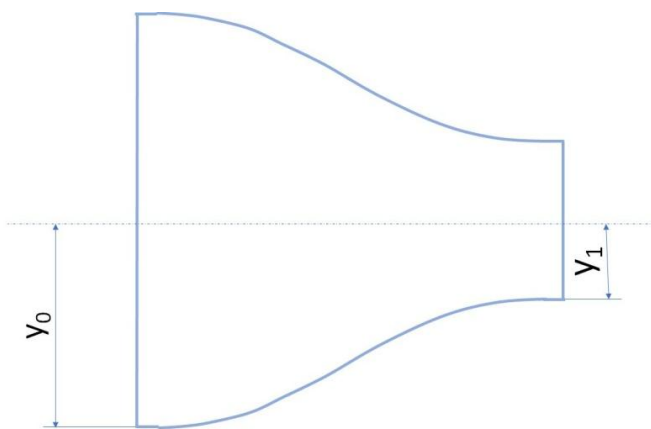
Figure 2: Nozzle shape

$$\xi = 0 \ \longrightarrow y = y_0 \qquad (7)$$

$$\xi = 1 \ \longrightarrow y = y_1 \qquad (8)$$

$$\xi = 0 \ \longrightarrow \frac{dy}{d\xi} = 0 \qquad (9)$$

$$\xi = 1 \ \longrightarrow \frac{dy}{d\xi} = 0 \qquad (10)$$

$$\xi = 0 \ \longrightarrow \frac{d^2y}{d\xi^2} = 0 \qquad (11)$$

$$\xi = 1 \ \longrightarrow \frac{d^2y}{d\xi^2} = 0 \qquad (12)$$

Considering the semi side-length of inlet cross-section y_0 and the semi side-length of outlet cross-section y_1 the Bell-Metha polynomials coefficients are reported in Table 1.

Table 1: Bell-Metha polynomials coefficients

Coefficient	Value
a_1	$-18.9\bar{9} \ (y_1 - y_0)$
a_2	$1.6\bar{6} \ (y_1 - y_0)$
a_3	$18.3\bar{3} \ (y_1 - y_0)$
a_4	0
a_5	0
C	y_0

According to the studies of Bell and Metha [[15]], a wind tunnel contraction should have a total length and a double semi side-length of the inlet cross-section ratio about equal to 1 (see Eq. (13)).

$$\frac{L}{2y_0} \cong 1 \qquad (13)$$

Taking into account the experimental tests carried out by Bell and Metha [[15]], a ratio less than 0.667 leads to an air flow detach just before the contraction outlet cross-section, while a ratio greater than 1.79 leads to an increase in boundary layer thickness. As best practice, a ratio value of 0.9 may be a good trade-off. Therefore, using Eq. (13) the nozzle total length is calculated.

Settling chamber design

The settling chamber design is related to the components that the settling chamber is joined to. In an open-loop wind tunnel the settling chamber cross-section is equal to the contraction inlet cross-section and it is constant. The aim of this component is to calm down the flow velocity and to reduce flow turbulence before the flow enters the contraction.

First diffuser design

The design of the first diffuser starts from its inlet cross-section. The area and the shape are known as they are equal to the ones of the test chamber. In the case of open-circuit wind tunnel, the first diffuser is connected to the fan. Therefore, the

first diffuser outlet cross-section area is equal to the one of the fan. A connection element is needed in the case of different shapes.

To determine the fan cross-section area, a ratio between fan cross-section area and test chamber cross-section area AR should be imposed. According to [[15]], this ratio should be between 2 and 3 (see Eq. (14)).

$$2 \leq AR = \frac{\Omega_{fan}}{\Omega_{TS}} \leq 3 \qquad (14)$$

A value greater than 3 should be avoided in order to limit irregular flow velocity at the fan inlet section, while ratios less than 2 lead to an increase of the overall wind tunnel dimensions and costs. The best choice is a ratio equal to 2 which lead to lower wind tunnel dimensions and construction costs with a regular flow velocity at the fan inlet section.

The air velocity at fan outlet section can be evaluated by Eq. (15), knowing the area ratio and applying the Mass Conservation Law.

$$c_{fan} = \frac{1}{2} c_{TS} \qquad (15)$$

Moreover, the fan diameter can be determined using Eq. (16), knowing the area ratio and the outlet first diffuser cross-section area.

$$D_{fan} = 2 \sqrt{\frac{AR \; \Omega_{TS}}{\pi}} \qquad (16)$$

As far as the first diffuser total length calculation is concerned, cone expansion is imposed. Following the usual design rule in subsonic diffusers, the cone expansion should not exceed a maximum value of 6° [[14]].

The first diffuser inlet cross-section area is equal to the test section one, while the first diffuser outlet cross-section area is equal to the fan's inlet. Thus these are known values at this stage of the design process.

Once known the hydraulic diameters of the inlet and outlet diffuser cross-sections, the equivalent cone expansion angle can be calculated with Eq. (17).

$$\vartheta_e = \arctan\left(\frac{1}{2} \frac{\sqrt{AR} - 1}{\frac{L_{I\,Diff}}{D_h}}\right) \qquad (17)$$

Very long diffusers lead to high pressure losses. Thus, a 4° cone expansion is a good choice. This value is used in the National Full-Scale Aerodynamics Complex design at NASA Ames Research Center [[16]]. This fact endorses the choice made. Solving Eq. (17) for $L_{I\,Diff}$, the diffuser length can be calculated.

In the case of square diffuser cross-section shape, the side of the outlet cross-section is be determined by equalling the two areas (see Eq. (18)).

$$l_{I\,Diff} = \frac{\sqrt{\pi}}{2} D_{fan} \qquad (18)$$

Honeycomb design

In order to reduce the fluctuations in the transverse velocity, a honeycomb with cells aligned to the flow direction are used [[17]]. The effects of the honeycomb presence on the stream-wise velocity are minimal thanks to the very small pressure drop trough the honeycomb structure.

As far as the design method is concerned, the honeycomb length, the cell hydraulic and the porosity are design key factors [[18]].

The honeycomb porosity is the ratio between the actual flow cross-section area and the total cross-section area and it is expressed by Eq. (19).

$$\beta_h = \frac{\Omega_{flow}}{\Omega_{tot}} \qquad (19)$$

Two main conditions must be verified in the honeycomb design [[18]]. The honeycomb length and cell hydraulic diameter ratio must be in the range between 6 to 8 and the honeycomb porosity should be greater than 0.8 (see Eq. (20) and Eq. (21))

$$6 \leq \frac{L_{honey}}{D_{h\,honey}} \leq 8 \qquad (20)$$

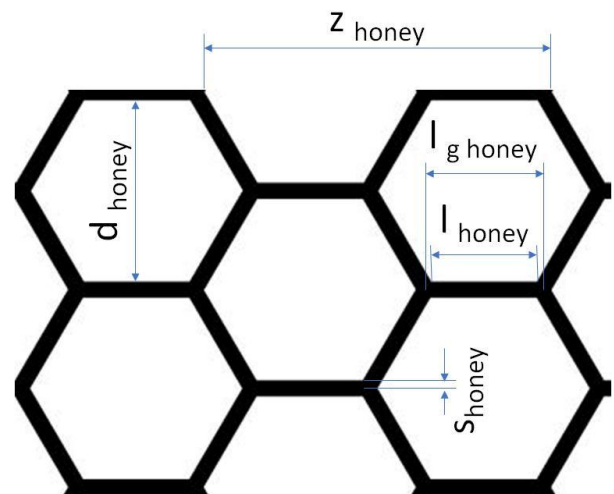$$\beta_h \geq 0.8 \qquad (21)$$

Figure 3: Honeycomb structure

According to Fig. 3, the honeycomb is defined by its geometric dimensions: inside honeycomb cell length l_{honey}; outside honeycomb cell length $l_{g\ honey}$; honeycomb cell diameter d_{honey}; honeycomb cell thickness s_{honey}; honeycomb solid sheet divisions z.

Basing on simple geometric considerations, the internal and external honeycomb cell lengths may be determined thorough Eq. (22) and Eq. (23), respectively.

$$l_{honey} = \frac{d_{honey}}{2 \sin 60°} \tag{22}$$

$$l_{g\ honey} = l_{honey} + 2 \frac{s_{honey}}{\tan 60°} \tag{23}$$

Using the same method, the solid sheet divisions can be easily evaluated (see Eq. (24)).

$$z_{honey} = 2\,l_{honey} + 2\,l_{g\ honey} \tag{24}$$

In order to calculate the solid area of the honeycomb, considering a single division, the solid area is the sum of two rectangular areas and two trapezoidal areas (see Fig. 3). These areas can be calculated using Eq. (25) and Eq. (26).

$$S_{rectangle} = l_{honey}\,s_{honey} \tag{25}$$

$$S_{trapeze} = \frac{\left(l_{honey} + l_{g\ honey}\right) s_{honey}}{2} l_{honey} + l_{g\ honey} \tag{26}$$

The number of divisions height-wise and width-wise are necessary to determine the honeycomb porosity. The number of divisions height-wise is defined as the ratio between the settling chamber cross-section height and the honeycomb divisions, as showed in Eq. (27).

$$n_z = \frac{h_{SC}}{z_{honey}} \tag{27}$$

The number of divisions width-wise is the ratio between the settling chamber cross-section width and the sum of honeycomb cell thickness and the half honeycomb cell diameter (see Eq. (28)).

$$n_{sheet} = \frac{L_{SC}}{s_{honey} + \frac{d_{honey}}{2}} \tag{28}$$

It is evident that for square cross-section Eq. (29) comes out.

$$h_{SC} = L_{SC} \tag{29}$$

Therefore, the cross-section area of the honeycomb solid sheet is calculated using Eq. (30).

$$\Omega_{sheet} = 2\left(S_{rectangle} + S_{trapeze}\right) n_z\, n_{sheet} \tag{30}$$

In a dual way, it is possible to define the honeycomb solidity as the ratio between the cross-section area of the solid sheet and the settling chamber cross-section area. According to the solidity definition, Eq. (31) comes out.

$$\sigma_h = \frac{\Omega_{sheet}}{\Omega_{tot}} \tag{31}$$

Comparing Eq. (31) and Eq. (19), it is easy to achieve the conclusion that the honeycomb and porosity are complementary factors. Thus, Eq. (32) comes out.

$$\sigma_h + \beta_h = 1 \tag{32}$$

Therefore, knowing the honeycomb solidity, the porosity can be calculated using Eq. (32). Thus, the criterion expressed in Eq. (21) is verified.

In the honeycomb, the design criterion in Eq. (20) should be verified. Thus, the cell hydraulic diameter should be calculated. Firstly, the cell area is calculated using Eq. (33).

$$\Omega_{cell} = 6\left(\frac{d_{honey}}{2} \frac{l_{honey}}{2}\right) = 6\,\frac{d_{honey}}{2} \frac{d_{honey}}{2\sqrt{3}} = \frac{3}{2} \frac{d_{honey}^2}{\sqrt{3}} \tag{33}$$

Areas equality is used (see Eq. (33 a)) to determine the cell hydraulic diameter.

$$\pi \frac{D_{h\ honey}^2}{4} = \Omega_{cell} = \frac{3}{2} \frac{d_{honey}^2}{\sqrt{3}} \tag{33 a}$$

Thus, Eq. (34) comes out and the cell hydraulic diameter can be obtained.

$$D_{h\ honey} = d_{honey} \sqrt{\frac{6}{\pi \sqrt{3}}} \tag{34}$$

Both the criteria expressed by Eq. (20) and Eq. (21) must be verified at the end of the honeycomb design procedure.

Screens design

In order to reduce stream-wise velocity fluctuations, screens must be introduced in the main stream direction. The screens

have great influence on velocity fluctuations and negligible effects on flow direction [[17]]. According to Prandtl [[17]], a series of screens with different mesh quality are more efficient than a single screen for the turbulence reduction.

The main factor which has the greater impact on screen effectiveness is the screen porosity, which is usually defined as the actual flow area and total area ratio [[1], [14]].

$$\beta_s = \frac{\Omega_{flow}}{\Omega_{tot}} \qquad (35)$$

Therefore, the screens effectiveness in reducing turbulence is strictly related to its porosity, which should be in the range between $0.58 - 0.8$, as showed in Eq. (36) [[18]]. The range ends choice is related to the flow instability induction (lower end) and turbulence control (upper end) [[17]].

$$0.58 \leq \beta_s \leq 0.8 \qquad (36)$$
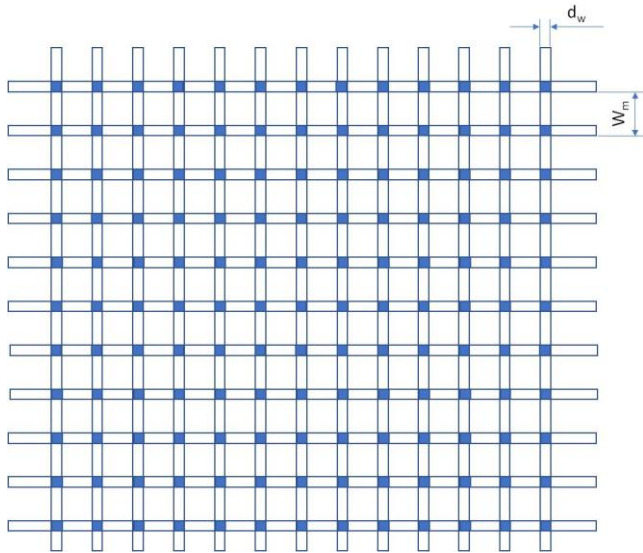
Figure 4: Screen structure

As a general rule, screens should be installed on removable frames to allow for cleaning and maintenance.

According to Fig. 4, it is possible to evaluate the screen porosity calculating the area occupied by the wires using Eq. (37), for the case of screen installed into square settling chamber and the commonest case of square mesh.

$$n_w L_{SC} d_w + n_w L_{SC} d_w - n_w(n_w d_w^2) \qquad (37)$$

The screen porosity can be evaluated by means of Eq. (38).

$$\beta_s = \frac{\Omega_{flow}}{\Omega_{tot}} = \frac{L_{SC}^2 - 2\,n_w L_{SC} d_w + n_w^2 d_w^2}{L_{SC}^2}$$
$$= 1 - 2\,n_w \frac{d_w}{L_{SC}} + \frac{n_w^2\,d_w^2}{L_{SC}^2} \qquad (38)$$

From Eq. (38), Eq. (39) easily comes out.

$$\beta_s = \left(1 - \frac{n_w d_w}{L_{SC}}\right)^2 \qquad (39)$$

WIND TUNNEL TEST CASE

In the present work, a very small-scale open-loop wind tunnel was designed and built in order to test the quality of the design criteria. Moreover, the aim of the present paper is to verify if a wind tunnel of that scale is suitable for studies on aerofoil flow-field behaviour.

As far as the testing chamber characteristics (dimensions and shape) is concerned, a square cross-section shape with 45° chamfers, a side of 5 cm and a length of 11.3 cm (length set to twice the hydraulic diameter) was built. In Fig. 5 the test chamber during a construction step is shown.
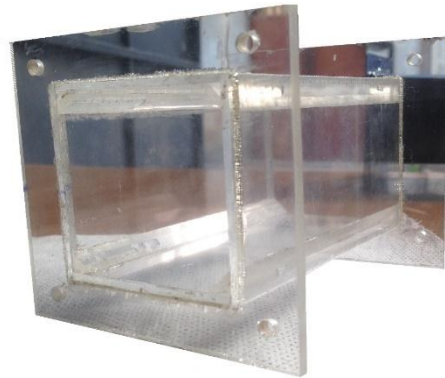
Figure 5: Small-scale wind tunnel test chamber

In the present wind tunnel design, a contraction area ratio of 7 was chosen, while the ratio between the contraction length and double semi side-length of inlet cross-section of 0.91 was set. These choices lead to a nozzle length of 13 cm, while the Bell-Metha polynomials coefficients are those reported in Table 1. Fig. 6 shows the contraction built.
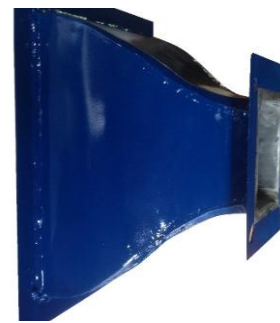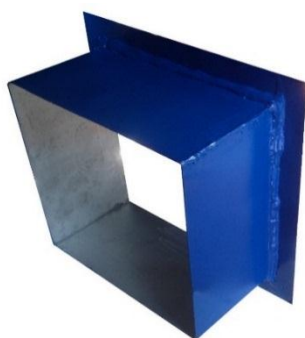

Figure 6: Small-scale wind tunnel contraction

The designed settling chamber had the same cross-section area and shape of the nozzle inlet cross-section as well as the

same length. In Fig. 7 the built settling chamber is shown.

Figure 7: Small-scale wind tunnel settling chamber

On the basis of the design procedure and recommendations, the first diffuser (see Fig. 8) should not exceed an expansion angle of 6°. In the present work, an angle of 4° was chosen. Thus, the first diffuser inlet cross-section had the same dimensions and shape of the testing section, while its outlet cross-section had a side of 71 mm. The first diffuser total length was 332 mm.

Figure 8: Small-scale wind tunnel first diffuser

Part of the settling chamber is occupied by the honeycomb. With reference to symbols reported in Fig. 3, in Table 2 the main honeycomb characteristics are reported. The honeycomb was 3D printed and it is made of PLA. The designed and built honeycomb of the present test case is shown in Fig. 9.

Figure 9: Small-scale wind tunnel honeycomb

Table 2: Honeycomb main characteristics

| Description	Symbol	Value
Cell diameter	d_{honey}	9 mm
Sheet thickness	s_{honey}	0.4 mm
Roughness	Δ	15 mm
Length	L_h	62 mm
Honeycomb cell side	l_{honey}	5.20 mm
External cell side	$l_{g\,honey}$	5.26 mm
Divisions	z_{honey}	15.66 mm
Honeycomb porosity	β_h	0.9825
Cell hydraulic diameter	D_h	9.45 mm
Length-hydraulic diameter ratio	L_h/D_h	6.56

Figure 10: Small-scale wind tunnel fan

As far as the fan choice is concerned, a commercial available fan was chosen. The main characteristics of this fan are reported in Table 3, while Fig. 10 shows the fan inside the wind tunnel case. In Fig. 11 the assembly of the small-scale open-loop wind tunnel is shown.

Table 3: Main wind tunnel fan characteristics

Description	Value
Power	28.8 W
Supply tension	240 V
Supply current	0.12 A
Supply frequency	50 Hz
Volumetric flow	175 m³/h
Outlet pressure	44 Pa
Speed	2100 r/min
Outlet diameter	98 mm
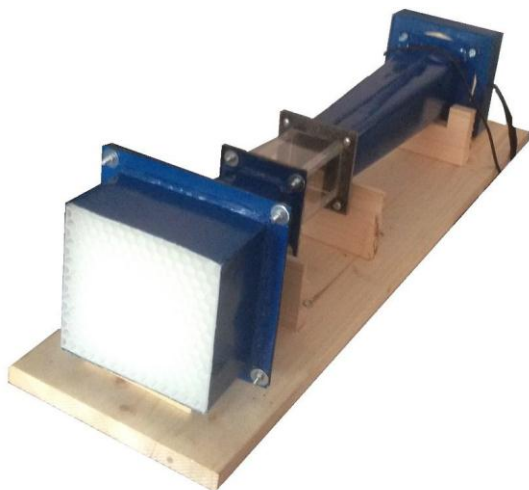
Figure 11: Small-scale wind tunnel assembly

## EXPERIMENTAL SETUP AND METHODS

In order to test and evaluate the potentiality of the small-scale wind tunnel, a specific experimental setup was implemented. The main instrument in the experimental setup is the Particle Image Velocimetry (PIV) which allow for inflow and velocity flow-field measurements within the wind tunnel test section [[19]]. Velocity field and flow parameters in the whole test chamber can be derived using this technique.

Particle Image Velocimetry is an optical, not in contact, measurement method for the visualization and measurement of flow-fields. This method is widely used to obtain instantaneous velocity measurements and related fluid properties. The fluid must to be seeded with small tracing particles, which are assumed to realistically follow the flow dynamics (the Stokes number is the degree for which the particles faithfully follow the flow).

As far as the seeding is concerned, an air assisted atomizer was used to create small oil droplets in the flow field. The Stokes number of the seeding was maintained lower than 0.1, so that the oil droplets closely follow the fluid streamlines.

Ion laser illuminates the fluid and the entrained particles, so that particles become visible. Dual frame cameras register images sequence and the motion of the seeding particles is used to calculate velocity and direction (the velocity field) of the flow. In Fig. 12 a simplified PIV measurement scheme is reported.

Moreover, at the end of each wind tunnel components, pressure transducers were installed and pressure differential between inlet and outlet flow were measured to calculate pressure drop for each wind tunnel component. In this study, Trafag MIT-12-8473_100mbar ceramic relative pressure transducers, with a measurement range from 0 to 0.1 bar with an accuracy of ±0.2% of full-scale, were used.
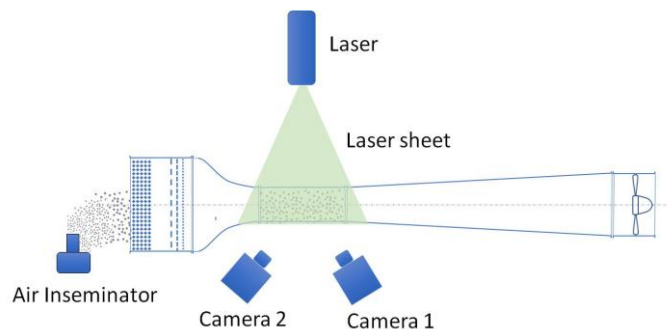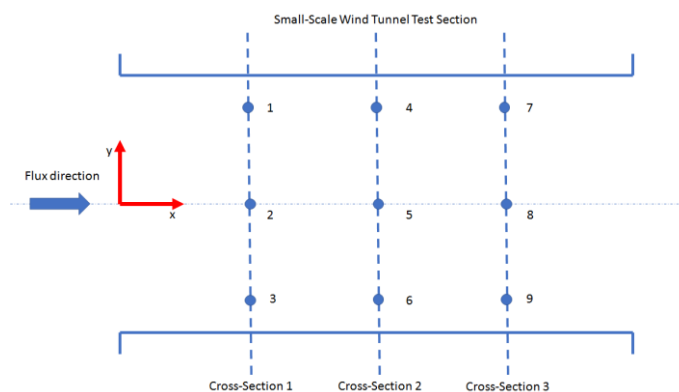

Figure 12: PIV measurement scheme

Figure 13: Experimental setup

Pressure signals were acquired by means of NI CompactDAQ, cDAQ-9178 [[20]] measurement system with NI 9203 +/-20 mA, 16-Bit, 200 kS/s, 8-Ch AI Module [[21]]. A personal computer was used to acquire signals with NI CompactDAQ system using NI Labview software [[22]].

In Fig. 13 an image of both the built small-scale wind tunnel and the experimental setup is shown.

In order to verify the reliability of the design and the construction of the wind tunnel, a measurement campaign using the optical methods was carried out. Specifically, Particle Image Velocimetry was used to measure flow velocity field into the wind tunnel test section and to calculate velocity profiles, turbulence intensities and others flow characteristics.

Figure 14: Measurement points scheme

Nine measurement points were located in the test section longitudinal symmetry plane (see Fig. 14) to calculate turbulence intensity along the flux direction. Moreover, velocity profile in the same three test chamber cross-sections (close to the inlet section, in the middle of the test section and close to the outlet section) were determined.

According to Fig. 14, Table 4 and Table 5 report the coordinates in terms of chamber hydraulic diameter of the nine measurement points and of the three test chamber cross-sections, respectively.

Table 4: Measurement points coordinates (see Fig. 14)

Measurement Point	Coordinate x	Coordinate y
Point 1 (P1)	0.5 D_h	0.25 D_h
Point 2 (P2)	0.5 D_h	0 D_h
Point 3 (P3)	0.5 D_h	-0.25 D_h
Point 4 (P4)	1.0 D_h	0.25 D_h
Point 5 (P5)	1.0 D_h	0 D_h
Point 6 (P6)	1.0 D_h	-0.25 D_h
Point 7 (P7)	1.5 D_h	0.25 D_h
Point 8 (P8)	1.5 D_h	0 D_h
Point 9 (P9)	1.5 Dh	-0.25 Dh

Table 5: Measurement test chamber cross-sections coordinates

Cross-Sections	Coordinate
Cross-section 1 (CS1)	0.5 D_h
Cross-section 2 (CS2)	1.0 D_h
Cross-section 3 (CS3)	1.5 D_h

For each measurement point, average velocities were determined by means of Reynold averaging method [[23]]. In the same measurement points turbulence intensity was calculated using Eq. (39), Eq. (40) and Eq. (41)

$$I = \frac{u'}{U} \tag{39}$$

$$u' = \sqrt{\frac{1}{2}\left(u'^2_x + u'^2_y\right)} \tag{40}$$

$$U = \sqrt{U_x^2 + U_y^2} \tag{41}$$

Specific attention was made for air seeding. The measurements were started waiting the complete quiescence of the oil droplets at the wind tunnel entrance so as the flow conditions were not perturbed by air-assisted atomizer stream.

WIND TUNNEL QUALIFICATION

Using the experimental setup and methods described above, a test of the proposed small-scale open-loop wind tunnel was carried out. In particular, the velocity field within the test chamber was measured using Particle Image Velocimetry and air stream parameters were extracted.


**Figure 15:** Velocity field within testing chamber

As an example, in Fig. 15 air velocity flow field within the test chamber is reported, while in Fig. 16, 17 and 18 Turbulence Intensity (TI) and Reynolds averaged air velocity, determined for measurement points (see Fig. 14 and Table 4), are shown. The measures of the air stream were made in the test section in a longitudinal symmetry plane. The analysis of the image in Fig. 15 highlights that the air velocity vectors are sufficiently well aligned with the chamber x-direction, while at the end of the test chamber some vectors deviations are registered.

(a)   (b)
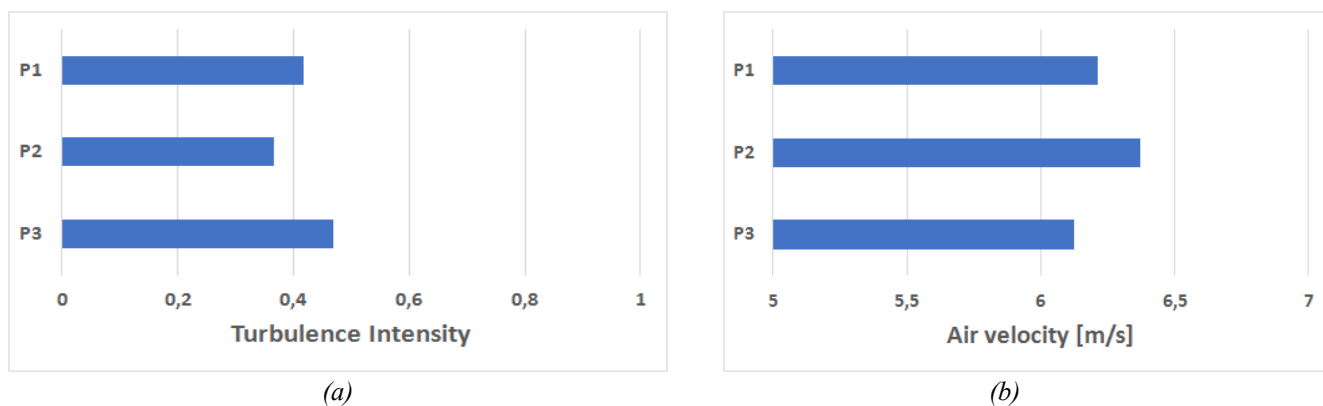
Figure 16: Turbulence intensity and mean velocity in points 1 to 3

(a)   (b)
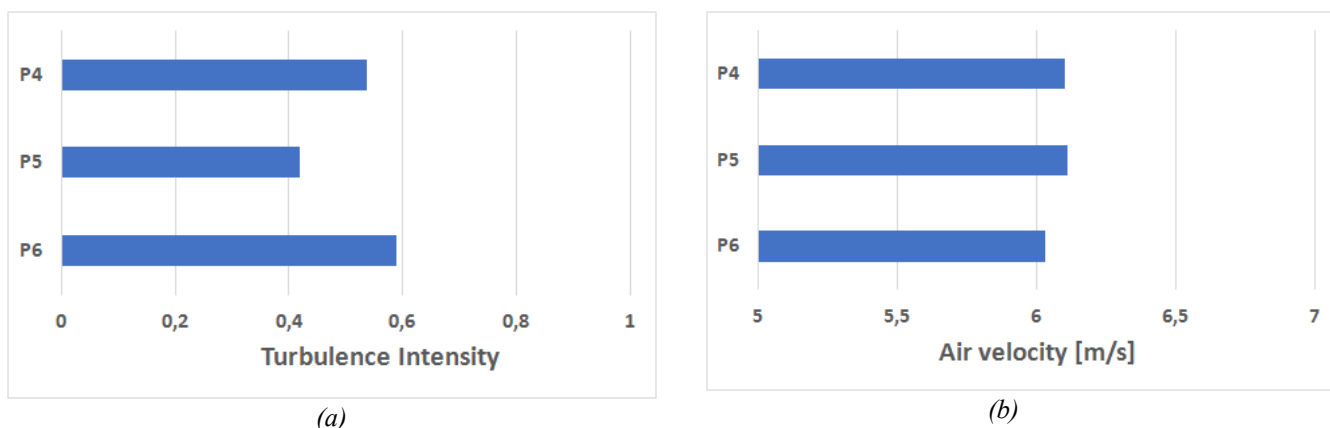
Figure 17: Turbulence intensity and mean velocity in points 4 to 6

(a)   (b)
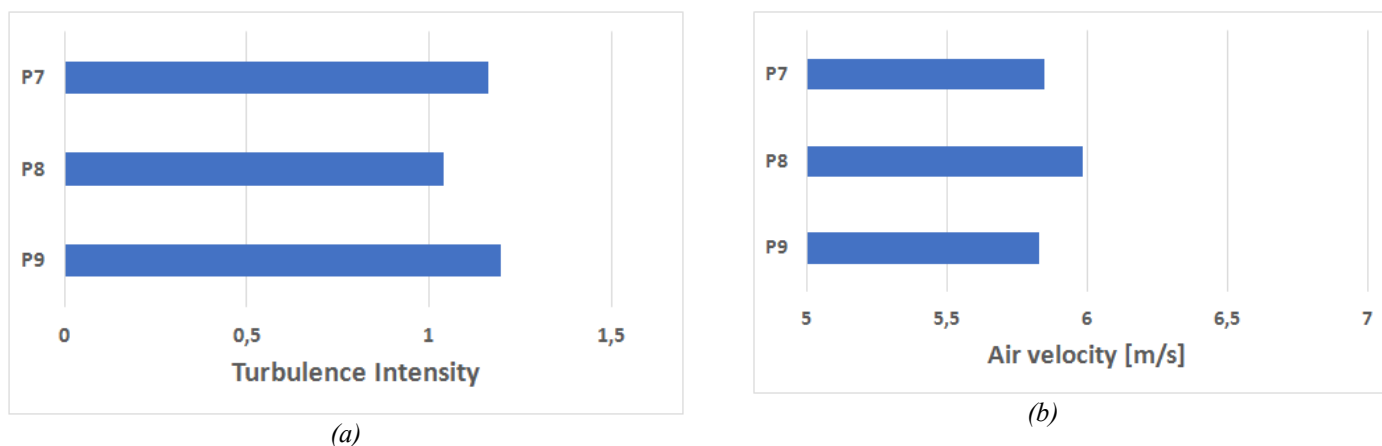
Figure 18: Turbulence intensity and mean velocity in points 7 to 9

This is also confirmed by the results reported in Fig. 16(a), 17(a) and 18(a). At the end of the test section an increase in Turbulent Intensity (about 1 %) is registered (Fig. 18(a)), while at the beginning of the test section a turbulent intensity of about 0.4 % is obtained (see Fig. 16(a) and Fig. 17(a)). This negative effect is probably due to the fan vorticity interaction with the flow field within test outlet section. The problem may probably be reduced using a second settling chamber between first diffuser and fan section.

A mean velocity (Reynolds averaged) of about 6 m/s was measured along the test section with a slight reduction in the higher turbulence zone (see Fig. 16(b), 17(b) and 18(b)).

In Fig. 19, 20 and 21 the air velocity in measurement points as a function of time are reported. As it is well observed in Fig. 19, air velocity is almost regular and the higher magnitude is registered at the middle of the test section. Going through from inlet to outlet section, turbulence intensity increases and
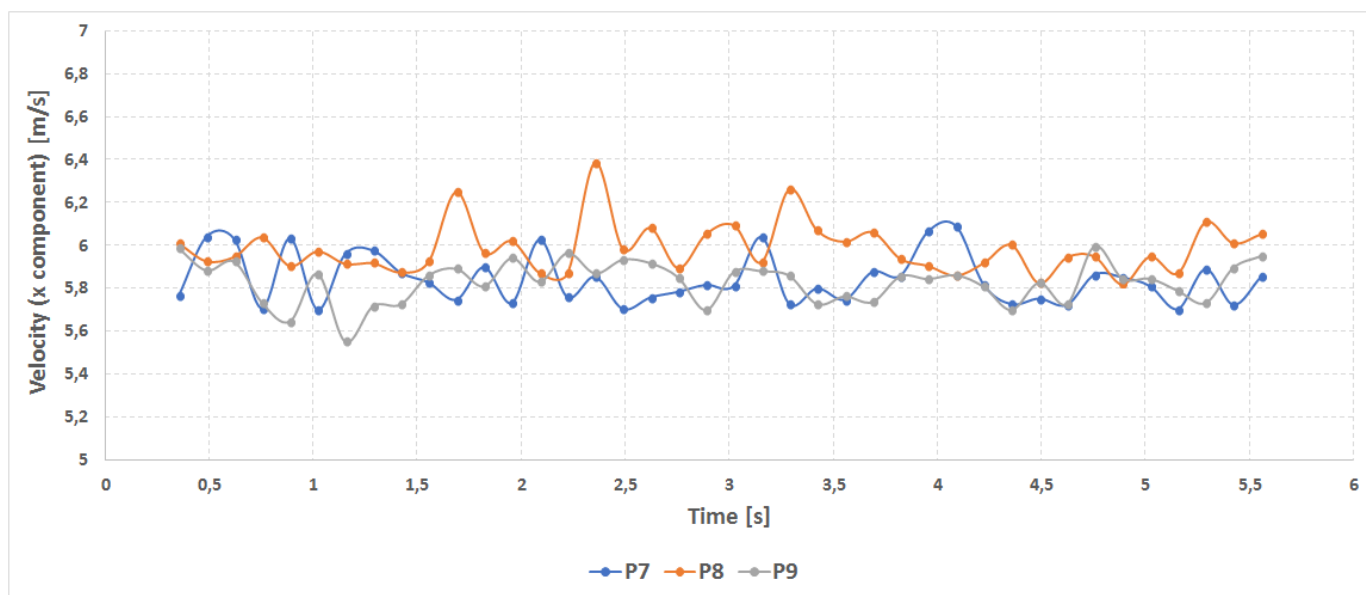
this is evident in Fig. 21. The higher the turbulence intensity,
more overlapped the curves are.
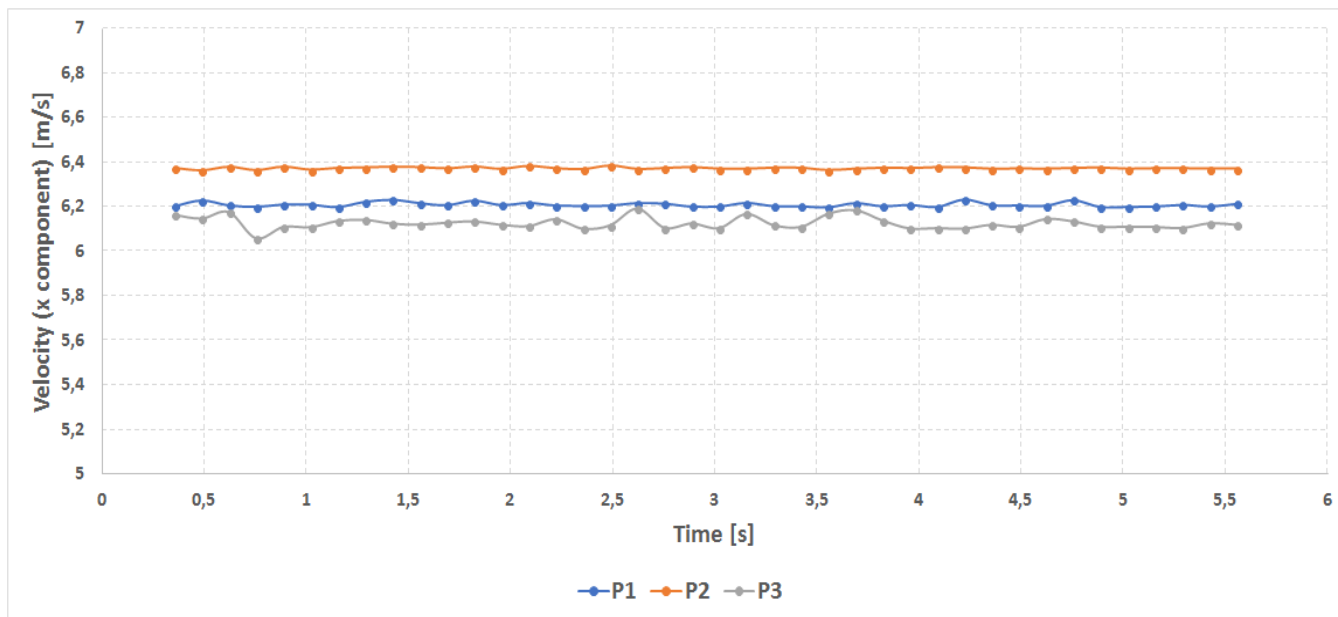
Figure 19: Instantaneous air velocity in the x-direction in measurement points 1, 2 and 3
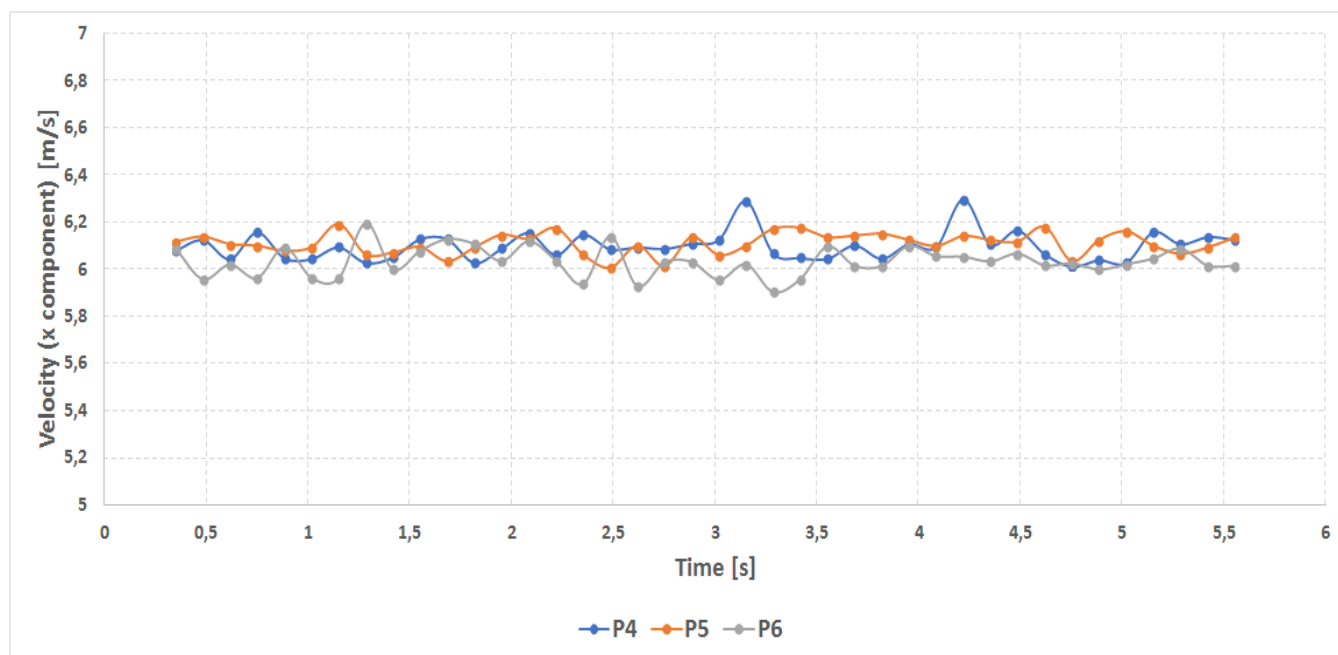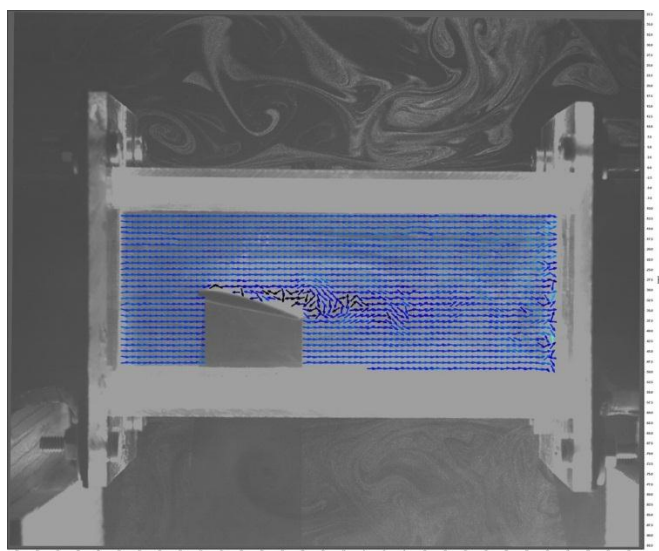

Figure 20: Instantaneous air velocity in the x-direction in measurement points 4, 5 and 6

Figure 21: Instantaneous air velocity in the x-direction in measurement points 7, 8 and 9

As an example of the designed small-scale open-loop wind tunnel potentialities, velocity field around a NACA0012 aerofoil during a wind tunnel tests is reported in Fig. 22. As it is possible to observe in the figure, flow detaching from the aerofoil surface is well evident, while a wake is visible at the aerofoil trailing edge. The image in Fig. 22 demonstrate that the small-scale wind tunnel may be used to measure the flow field and its characteristics in many scientific and practical aerodynamics problems [24, 25, 26]. For example, the optical wind tunnel experimental data can be used in order to calibrate and verify Computational Fluid Dynamics models. Therefore, for example, these data are very useful in studies of small drone propellers aerofoils design or micro wind turbines.

CONCLUSIONS

In the present work, the design procedure of a small-scale open-loop wind tunnel is described. Moreover, measurement techniques based on PIV are shown. Indeed, in order to test the design procedure and measurement technique, a very small-scale open-loop wind tunnel was designed and built. A Particle Image Velocimetry experimental setup was implemented and used to qualify the built wind tunnel.

The experimental results in the wind tunnel qualification tests highlighted that the proposed wind tunnel had a test section flow velocity of 6 m/s with a relatively small turbulence level (about 0.4 %). A slight increase in the turbulence level along the test section was registered. The maximum measured turbulence intensity was about 1 % at the test section outlet. This is probably due to the interaction between fan flow structure and test section flow-field. This effect may probably be reduced by extending the wind tunnel length, with a settling chamber between the first diffuser and the fan section. However, the overall quality of the proposed small wind tunnel appear to be suitable for low Re aerodynamics study such as aerofoils, micro wind turbine rotors, small drones and similar. This is also due to the wide possibilities offered by PIV.

In conclusion, the experimental data demonstrate that a small-scale wind tunnel may be more easily used to measure the flow field and its characteristics around low Re aerofoils than the large wind tunnel. Indeed, a small-scale wind tunnel is certainly more suitable for PIV optical techniques thanks to its reduced dimensions and easy flow seeding.

Figure 22: Velocity field around NACA0012 aerofoil

NOMENCLATURE

UAV	Unmanned Air Vehicle
MAV	Micro Air Vehicle
WT	Wind Turbine
Ω_{TS}	Test section cross-sectional area
D_h	Test section equivalent hydraulic diameter
L_h	Test section length
L	Total nozzle length
a_i	Bell-Metha polynomial coefficients
h	Half cross-section side-length
y_0	Semi side-length of inlet cross-section
y_1	Semi side-length of outlet cross-section
$L_{I\,Diff}$	First diffuser total length
Ω_{fan}	Fan cross-sectional area
AR	Fan cross-section area and test chamber cross-section area ratio
c_{fan}	Velocity at the fan outlet section
c_{TS}	Velocity at the test section
$l_{I\,Diff}$	First diffuser side
h_{honey}	Honeycomb length
$D_{h\,honey}$	Honeycomb cell hydraulic diameter
β_{honey}	Honeycomb porosity
l_{honey}	Inside honeycomb cell length
$l_{g\,honey}$	Outside honeycomb cell length
d_{honey}	Honeycomb cell diameter
s_{honey}	Honeycomb cell thickness
z_{honey}	Honeycomb solid sheet divisions
h_{SC}	Settling chamber cross-section height
L_{SC}	Settling chamber cross-section width
n_z	Number of divisions height-wise
n_{sheet}	Number of divisions width-wise
β_s	Screen porosity
d_w	Screen wire diameter
n_w	Screen wire number
P_i	i-th measurement point
CS_i	i-th measurement test chamber cross-section
TI	Turbulence Intensity

REFERENCES

[1] Serdar Genç M., İlyas Karasu, Hakan Açıkel H. An experimental study on aerodynamics of NACA2415 aerofoil at low Re numbers. Experimental Thermal and Fluid Science, Vol. 39, pp. 252-264, 2012. DOI: 10.1016/j.expthermflusci.2012.01.029

[2] Ricci R., Montelpare S. A. Quantitative IR thermographic method to study the laminar separation bubble phenomenon. International Journal of Thermal Sciences, Vol. 44, pp. 709–719, 2005. DOI: 10.1016/j.ijthermalsci.2005.02.013

[3] Ricci R., Montelpare S. A., Silvi E. Study of acoustic disturbances effect on laminar separation bubble by IR thermography. Experimental Thermal and Fluid Science, Vol. 31, pp. 349–359, 2007. DOI: 10.1016/j.expthermflusci.2005.08.007

[4] Zhang W., Hain R., Kahler C. J. Scanning PIV investigation of the laminar separation bubble on a SD7003 airfoil. Experiment in Fluids, Vol. 45, pp. 725–743, 2008. DOI: 10.1007/s00348-008-0563-8

[5] Mellen C.P., Frohlich J., Rodi W. Lessons from lesfoil project on large-eddy simulation of flow around an airfoil. AIAA Journal, Vol. 41, pp. 573–581, 2003. DOI: 10.2514/2.2005

[6] Davidson L. LESFOIL: Large Eddy Simulation of Flow Around a High Lift Airfoil: Results of the Project LESFOIL Supported by the European Union 1998-2001, Vol. Springer, 2003. ISBN 978-3-540-36457-3

[7] A. Uranga A., Persson P.O., Drela M., Peraire J. Implicit large eddy simulation of transitional flows over airfoils and wings. Proceedings of the 19th AIAA Computational Fluid Dynamics, no. AIAA, 4131, 2009.

[8] Sarlak H., Mikkelsen R., Sarmast S., Sørensen J.N. Aerodynamic behavior of nrel s826 at re=100,000. Journal of Physics, Conf. Series, Vol. 524, pp. 012027, 2014. DOI: 10.1088/1742-6596/524/1/012027

[9] Sarlak H., Nishino T., Sørensen J. N, Simos T., Tsitouras C. Urans simulations of separated flow with stall cells over an nrel s826 airfoil. AIP Conference Proceedings, Vol. 1738, pp. 030039, 2016. DOI: 10.1063/1.4951795

[10] Rainbird J. M., Peiró J., Graham J. M. R. Blockage-tolerant wind tunnel measurements for a NACA 0012 at high angles of attack. Journal of Wind Engineering and Industrial Aerodynamics, Vol. 145, pp. 209-218, 2015. DOI: 10.1016/j.jweia.2015.06.006

[11] Bayati I., Belloli M., Bernini L., Zasso A. Aerodynamic design methodology for wind tunnel

tests of wind turbine rotors. Journal of Wind Engineering and Industrial Aerodynamics, Vol. 167, pp. 217-227, 2017. DOI: 10.1016/j.jweia.2017.05.004

[12] Celis B., Ubbens H. H. Design and Construction of an Open-circuit Wind Tunnel with Specific Measurement Equipment for Cycling. Procedia Engineering, Vol. 147, 2016, pp. 98-103, 2016. DOI: 10.1016/j.proeng.2016.06.196

[13] Brusca S., Lanzafame R., Messina M. Low-speed wind tunnel: Design and build Wind Tunnels: Aerodynamics, Models and Experiments. pp. 189-220, 2011. ISBN: 978-161209204-1

[14] Barlow J. B., Rae W. H. Jr.- Pope A. Low Speed Wind Tunnel Testing. 3rd Ed. Wiley-Interscience: New York, 1999. ISBN: 978-0-471-55774-6

[15] Bell J. H., Metha R. D. Contraction Design for Small Low-Speed Wind Tunnels. NASA-CR-182747, 1988.

[16] Zell P. Performance and Test Section Flow Characteristics of the National Full-Scale Aerodynamics Complex 80- by 120-Foot Wind Tunnel. NASA TM 103920, 1993.

[17] Prandtl L. Attaining a Steady Stream in Wind Tunnel NACA TM 726, Oct. 1933.

[18] Metha R. D., Bradshaw P. Design Rules for Small Low Speed Wind Tunnels. Journal of Royal Aeronautical Society 1979, Vol. 73. DOI: 10.1017/S0001924000031985

[19] Raffel M., Willert C., Wereley S., Kompenhans J. Particle Image Velocimetry: A Practical Guide. 2nd ed. Springer, 2007. ISBN 978-3-540-72308-0

[20] National Instruments, NI cDAQTM-9171/9174/9178 User Manual, 2016.

[21] National Instruments, NI 9203 8-Channel, ±20 mA, 16-Bit Analog Input Module User Manual, 2016.

[22] National Instruments, NI Labview User Manual, 2015.

[23] Davidson P. A. Turbulence, an introduction for scientists and engineers. Oxford University Press, 2009. ISBN 978-0198529491.

[24] R. Lanzafame, S. Mauro, M. Messina - Numerical and experimental analysis of micro HAWTs designed for wind tunnel applications - International Journal of Energy and Environmental Engineering - June 2016, Volume 7, Issue 2, pp 199–210 - DOI: 10.1007/s40095-016-0202-8

[25] S. Brusca, F. Famoso, R. Lanzafame, S. Mauro, M. Messina, S. Strano - PM10 Dispersion Modeling by Means of CFD 3D and Eulerian–Lagrangian Models: Analysis and Comparison with Experiments - Energy Procedia 101:329-336, November 2016 DOI: 10.1016/j.egypro.2016.11.042

[26] S. Brusca, F. Famoso, R. Lanzafame, S. Mauro, A. Marino Cugno Garrano, P. Monforte - Theoretical and Experimental Study of Gaussian Plume Model in Small Scale System - Energy Procedia 101:58-65 · November 2016 DOI: 10.1016/j.egypro.2016.11.008